Structural Disorder by Octahedral Tilting in Inorganic Halide Perovskites: New Insight with Bayesian Optimization

Jingrui Li, Fang Pan, Guo-Xu Zhang, Zenghui Liu, Hua Dong, Dawei Wang, Zhuangde Jiang, Wei Ren, Zuo-Guang Ye, Milica Todorović,* and Patrick Rinke*

Structural disorder is common in metal-halide perovskites and important for understanding the functional properties of these materials. First-principles methods can address structure variation on the atomistic scale, but they are often limited by the lack of structure-sampling schemes required to characterize the disorder. Herein, structural disorder in the benchmark inorganic halide perovskites $CsPbI_3$ and $CsPbBr_3$ is computationally studied in terms of the three octahedral-tilting angles. The subsequent variations in energetics and properties are described by 3D potential-energy surfaces (PESs) and property landscapes, delivered by Bayesian optimization as implemented in the Bayesian optimization structure search code sampling density functional theory (DFT) calculations. The rapid convergence of the PES with about 200 DFT data points in 3D searches demonstrates the power of active learning and strategic sampling with Bayesian optimization. Further analysis indicates that disorder grows with increasing temperature and reveals that the material bandgap at finite temperatures is a statistical mean over disordered structures.

Disorder phenomena are very common in emergent functional materials, as ion-mixing or doping strategies are widely applied to obtain high performance and stability. Notable examples include ferroelectric oxide perovskite solid solutions,[9–11] multiple-cation metal halide perovskites for solar cells and light-emitting diodes,[12,13] and kesterite photovoltaic materials.[14,15] Structural disorder can also occur in pure materials with perfect stoichiometry, if the material exhibits a series of stable structures with similar thermodynamic free energies and the energy barriers separating free-energy minima are easy to overcome. Consequently, properties of complex functional materials often arise from the thermal population of a number of low-energy structures.

1. Introduction

Structural disorder in materials has become an important topic in both experimental and computational materials science.[1–8]

Cesium lead iodide ($CsPbI_3$) is an example of the latter category that has received increasing attention in recent years. It is a promising photovoltaic material as $CsPbI_3$-based perovskite solar cells have a reported power conversion efficiency above 21% and good stability.[16] It is generally believed that $CsPbI_3$ adopts the cubic

---

J. Li, F. Pan, Z. Liu, W. Ren
State Key Laboratory for Manufacturing Systems Engineering
Electronic Materials Research Laboratory
Key Laboratory of the Ministry of Education
School of Electronic Science and Engineering
Xi'an Jiaotong University
Xi'an 710049, China
E-mail: jingrui.li@xjtu.edu.cn

G.-X. Zhang
MIIT Key Laboratory of Critical Materials Technology for New Energy Conversion and Storage
School of Chemistry and Chemical Engineering
Harbin Institute of Technology
Harbin 150001, China

The ORCID identification number(s) for the author(s) of this article can be found under https://doi.org/10.1002/sstr.202400268.

DOI: 10.1002/sstr.202400268

H. Dong
Key Laboratory for Physical Electronics and Devices of the Ministry of Education and Shaanxi Key Lab of Information Photonic Technique
School of Electronic Science and Engineering
Xi'an Jiaotong University
Xi'an 710049, China

D. Wang
School of Microelectronics and Key Lab of Micro-Nano Electronics and System Integration of Xi'an City
Xi'an Jiaotong University
Xi'an 710049, China

Z. Jiang
State Key Laboratory for Manufacturing Systems Engineering & International Joint Laboratory for Micro/Nano Manufacturing and Measurement Technology
Xi'an Jiaotong University
Xi'an 710049, China

Z.-G. Ye
Department of Chemistry and 4D LABS
Simon Fraser University
Burnaby, British Columbia V5A 1S6, Canada

α phase (space group $Pm\overline{3}m$) at high temperatures, which successively converts into the tetragonal β phase ($P4/mbm$) at 533 K and then to the orthorhombic γ phase ($Pnma$) at 448 K upon cooling.[17] The structural details of the β phase are not well established. In a joint experimental–theoretical study, Marronnier et al. analyzed the phonon instabilities of this phase.[18] Jinnouchi et al. related the phase transition to the change in the effective Cs^+ radius by thermal fluctuations.[19] Klarbring suggested that the macroscopic tetragonal phase consists of dynamically fluctuating orthorhombic structures.[20] Yang et al. further showed that some other low-symmetry structures are also involved.[21] Dynamical disorder has previously been found in other isostructural inorganic halide perovskites.[20,22–24] For example, a recent density functional theory (DFT) and molecular dynamics study indicated that the disorder in cubic $CsPbBr_3$ is closely related to the octahedral-tilting dynamics.[24] The nature of disorder in the high-temperature phases of inorganic halide perovskites remains unclear to date. It is thus important to tackle disorder given the link between the atomic structure and functional properties of materials. Better knowledge of the involved structures, energetics, and mechanisms of structural fluctuations is crucial to understand the atomistic origin of functional properties and to design the next-generation high-performance perovskites.

To gain theoretical insight into structural disorder and its energetics, it is useful to study the system's multidimensional potential energy surface (PES),[25,26] that is, the total energy as a function of the relevant degrees of freedom (DOFs) for disorder. Energy differences governing structural disorder may be very small, so we must employ accurate DFT methods which have celebrated great successes in modeling molecules and condensed matter systems.[27] DFT can supply 1D and 2D PESs with an equispaced-grid approach (such as in ref. [20]). Yet PES computations quickly become intractable as the number of DOFs and thus the number of grid points grows. Attempts to construct accurate high-dimensional PESs based on first-principles calculations can be traced back several decades, when a series of interpolation schemes were developed to study polyatomic chemical reactions.[28,29] However, it is not easy to directly apply this approach to complex-materials problems such as solid states and interfaces. Among the many atomic DOFs of a complex material, there are usually several "principal" DOFs that play a decisive role in structural energetics, while other DOFs are dependent or of secondary importance. As a result, such a PES could be much more complicated than that of a polyatomic molecular system. It might have multiple maxima and minima, making simple interpolation approaches difficult.

In the past decade, machine learning (ML) has made an impact in the field of computational materials science.[30–34] ML and DFT can be combined to approximate PESs[35,36] and to accelerate structure search with improved sampling schemes[37–41] and accelerated force evaluation.[42–45] Force fields can of course provide the PESs in terms of all atomic DOFs yet typically lack the accuracy. Modern machine-learnt force fields or interatomic potentials[46–53] also provide DFT accuracy, but they take a long time to train in materials with many chemical species. We are here, however, interested in PESs that we can visualize, which is not possible for high-dimensional PESs of force fields.

Recently, some of us have developed the Bayesian optimization structure search (BOSS) approach, an ML-based structure search scheme for accelerated and unbiased PES computation.[54] BOSS couples state-of-the-art DFT calculations with the active learning Bayesian optimization (BO) technique. It employs a Gaussian-process to fit a PES surrogate model to DFT data points and refines this model until convergence is achieved by acquiring further data with a smart sampling strategy. In such a way, BOSS can construct a complete high-dimensional PES using a relatively modest number of energy data points. BOSS has already been applied to solve problems such as conformer search for organic molecules[54,55] and adsorption of organic molecules at semiconductor surfaces,[54] to resolve different organic adsorbate types and film growth at metallic surfaces,[56–58] and to identify the interface geometries of inorganic or organic materials at perovskite surfaces.[59–61] The application of BO in materials science is not limited to structure search, for example, it was used to train the force fields to study phase transition in hybrid perovskites,[19] to select optimal ML hyperparameters,[62,63] or to efficiently solicit experimental data.[64,65]

In this work, we apply BOSS to study disorder in the benchmark systems $CsPbI_3$ and the isostructural bromide perovskite ($CsPbBr_3$). The latter is a standard green-emitting material for perovskite light-emitting diodes,[66] another of today's key materials in perovskite optoelectronics. We select the three octahedral-tilting angles[67] as the principal DOFs. Previous experimental and theoretical studies[20,22,24,68–70] have established that they are key to determining the materials structure. One of the main objectives of this work is to compute a realistic and accurate 3D PES that best reflects the structures inside the perovskite materials. The smart data sampling by BOSS enables us to include all three octahedral-tilting angles as variables for the 3D PES. We thus go beyond the previously established 2D view of Klarbring,[20] which nevertheless is considered as reference for our study. In addition we use BOSS to generate a 3D profile of the bandgap. This enables us to gain insight into the effects of structural disorder and temperature on functional properties. Important information about the structural disorder in both $CsPbI_3$ and $CsPbBr_3$ is obtained by gathering all these findings.

M. Todorović
Department of Mechanical and Materials Engineering
University of Turku
FI-20014 Turku, Finland
E-mail: milica.todorovic@utu.fi

P. Rinke
Department of Applied Physics
Aalto University
P.O.Box 11100, AALTO, FI-00076 Espoo, Finland

P. Rinke
Physics Department
TUM School of Natural Sciences
Technical University of Munich
Garching D-85748, Germany

P. Rinke
Munich Data Science Institute
Technical University of Munich
Garching D-85748, Germany

2. Bayesian optimization structure search scheme

2.1. Octahedral Tilting and the Disorder Search Spaces

The disorder search spaces for the benchmark systems $\mathrm{CsPbI_3}$ and $\mathrm{CsPbBr_3}$ are spanned by the three octahedral-tilting angles. We adopted the Glazer notation $a^{r_a}b^{r_b}c^{r_c}$ of octahedral tilting in perovskites[67] throughout this manuscript. Here, x^{r_x} denotes the tilt around the lattice vector x $(=a,b,c)$ of the quasicubic cell, and $r_x = +, -, 0$ indicates the in-phase, out-of-phase, and zero-tilting modes (sometimes shortened as “tilts”), respectively (**Figure 1**a). The corresponding tilting angle is denoted by θ_x hereafter. Different combinations of tilting modes and angles around the three lattice vectors result in different tilting patterns. The perovskite lattice accordingly exhibits different types of distortions. Originally, Glazer had derived 23 tilting patterns[67,71] and later Woodward revised this framework into 15 based on experimental results and space-group analysis.[72–74] In this work, we considered all possible tilting patterns (listed in **Table 1**) that are compatible with both Glazer’s and Woodward’s conventions. A recent study of $\mathrm{CsSnI_3}$, which is isostructural and closely related to our systems, indicates that this is necessary.[75] Results of full DFT relaxation for both systems with different tilting patterns are provided in Section S1, Supporting Information.

Table 1. Attribution of Glazer tilting patterns to different categories (disorder search spaces).

Tilting	ppp	ppm	pmm	mmm
$a^0a^0a^0$	✓	✓	✓	✓
$a^+b^0b^0$	✓	✓	✓	
$a^-b^0b^0$		✓	✓	✓
$a^+a^+c^0$, $a^+b^+c^0$	✓	✓		
$a^+b^-c^0$		✓	✓	
$a^-a^-c^0$, $a^-b^-c^0$			✓	✓
$a^+a^+a^+$, $a^+a^+c^+$, $a^+b^+c^+$	✓			
$a^+a^+c^-$, $a^+b^+c^-$		✓		
$a^+b^-b^-$, $a^+b^-c^-$			✓	
$a^-a^-a^-$, $a^-a^-c^-$, $a^-b^-c^-$				✓

The Glazer tilting patterns listed in Table 1 can be divided into four categories: those with three in-phase tilts, with two in-phase and one out-of-phase tilts, with one in-phase and two out-of-phase tilts, and with three out-of-phase tilts. For each of these, the three octahedral-tilting angles as coordinates span a 3D configuration space (Figure 1b). We denote them by $a^+b^+c^+$,

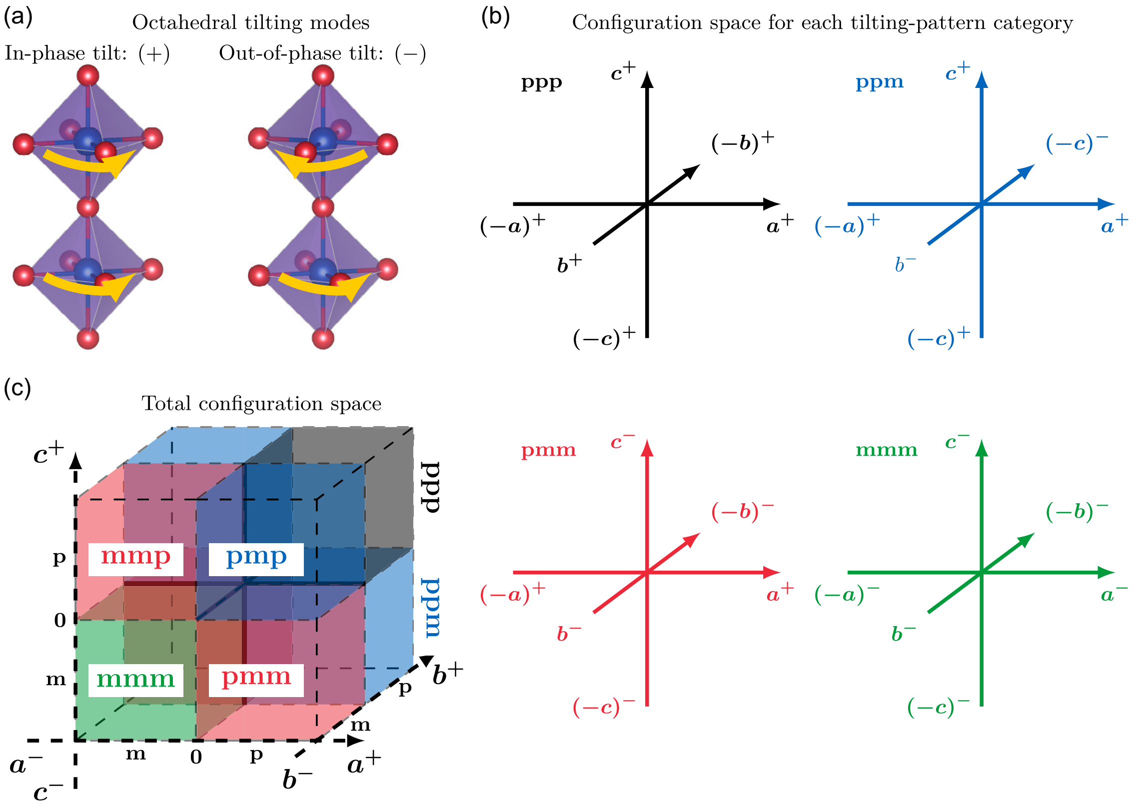

Figure 1. Definition of octahedral-tilting configuration spaces for $\mathrm{CsPbX_3}$ (X = I, Br) used in this work. a) Tilting modes along a lattice vector: in-phase tilt (left, Glazer notation “+”) and out-of-phase tilt (right, “−”), with $\mathrm{Pb^{2+}}$ cation colored in blue and $\mathrm{X^-}$ anions in red, octahedral rotation directions indicated by yellow arrows; b) the four configuration spaces representing different categories of octahedral-tilting patterns; and c) the total configuration space. Spaces in (b) and octants in (c) are colored to indicate the correspondence between them, for example, the “mmm” space in (b) and the “mmm” octant in (c) are both colored in green.

$a^+b^+c^-$, $a^+b^-c^-$, and $a^+b^+c^-$, or simply by ppp, ppm, pmm, and mmm, respectively, with "p" standing for plus ("+") and "m" for minus ("−"). For each of them, the "negative tilt" $(-x)^{r_x}$ describes the same tilt as the positive one, $(+x)^{r_x}$ (i.e., r_x mode by θ_x angle), but in the opposite direction.[20] We should note two important features of these configuration spaces: 1) tilting patterns with zero tilt(s) belong to more than one spaces, for example, $a^+b^+c^0$ belongs to both ppp and ppm, and 2) there are symmetry-equivalent points for each data point (except $a^0a^0a^0$). As a result, any of the eight octants of a configuration space, for example, octant I with $\theta_a \geq 0$, $\theta_b \geq 0$, $\theta_c \geq 0$, contains all information for this category. A brief discussion of symmetries for data points that represent different tilting patterns are supplied in Section S2, Supporting Information.

Figure 1c illustrates another way to construct the 3D disorder configuration space. All tilting patterns listed in Table 1 are included in one space by assigning the positive and negative values of each tilting-angle coordinate to in-phase and out-of-phase tilts, respectively. We thus refer to it as the "total configuration space" hereafter. The color correspondence between Figure 1b,c indicates that each of the eight octants of this total space can represent a tilting-pattern category. For example, points in the mmm octant, that is, $\theta_a \leq 0$, $\theta_b \leq 0$, $\theta_c \leq 0$, of this total space and points in the octant I of the mmm space represent identical structures. In addition, either ppm or pmm has two symmetry-equivalent octants in the total space.

2.2. BOSS Protocol

BOSS is an ML method that accelerates structure search via strategic sampling of the PES. In general, it can be used to rapidly explore *N*-dimensional domains and build surrogate models for any simulated properties. A more in-depth description of the BOSS scheme can be found in refs. [54,76,77]. Here we only outline the search principle of BOSS by highlighting the aspects that are different to earlier applications.

First, the structures were sampled separately in the ppp, ppm, pmm, and mmm search spaces to ensure that we have enough data for all four tilting-pattern categories. The 3D surrogate models for visualization and analysis, in contrast, were constructed within the total space to avoid ambiguous data at the subspaces (planes and lines) shared by different tilting-pattern categories. Second, for each arrangement of sampled tilting angles, we performed a full structural relaxation of all other DOFs. We opted for this approach instead of the building-block models in previous BOSS applications to release any strains or structural artefacts introduced by the rearrangement of perovskite octohedra. Third, we guaranteed that the surrogate models were constructed and the data acquired based on a set of DFT data points that reflect the structural symmetry of the materials as alluded to earlier. To this end, each sampling query additionally returned the data of all symmetry-equivalent points in the search space after each DFT calculation.

The BOSS workflow in this study is as follows. First, DFT calculations of tilted structures were separately sampled in each of the ppp, ppm, pmm, and mmm search spaces: 1) The database was initialized with three nonequivalent structures together with their symmetry images. 2) A 3D surrogate model was fit to all existing data using Gaussian process regression. 3) Based on the surrogate model, an acquisition function was calculated and used to determine the next sample point in the configuration space. 4) The database was updated with the newly sampled point and its symmetric images. 5) Steps 2–4 were repeated until the parameters of the most-stable structure did not change within 10 consecutive iterations (variation of total energy within 0.5 meV per perovskite unit and all tilting angles within 0.5°). Then the sampled data were merged into one data set according to the symmetry of the total configuration space. 3D surrogate models were fit to both DFT-calculated total energies and bandgaps to build the PESs and bandgap landscapes, respectively. The surrogate models for the band gap were obtained in the same way from the same set of computations.

Once the PES was evaluated, we analyzed it to extract the locations of all local minima and their predicted energies. For all minima, we removed the fixed tilting angle restriction and optimized the structures fully to evaluate the quality of this small approximation. For any pair of minima, we utilized the surrogate model to compute the minimum energy path (MEP) between them and determine the energies and structures of transition states.

For data sampling, we used the exploratory lower confidence bound[78] acquisition function which balances exploitation (search for better points near the predicted global minimum) and exploration (acquiring data in the less visited regions of the search space). Such heuristic approaches are suitable for an unbiased exploration of the entire configuration space, and not only limited to the vicinity of extrema.

For each sampled structure, we carried out DFT calculations for $CsPbX_3$ using a 2 × 2 × 2 supercell model that can host all Glazer tilting patterns. The Pb–X framework of the system was initialized according to the desired tilting pattern. The Cs locations and lattice parameters were relaxed during structural optimization, while the Pb and X fractional coordinates were frozen so that the tilting pattern was (at least approximately) maintained. We chose the Perdew–Burke–Ernzerhof exchange-correlation functional for solids (PBEsol)[79] and analytical stress tensor[80] implemented in the all-electron numeric-atom-centered orbital code FHI-aims,[81–84] as PBEsol describes the lattice constants of halide perovskites well with moderate computational cost.[85–87] Single-point bandgap calculations were performed for each optimized structure using a hybrid functional PBEsol0 that contains 25% exact exchange. Scalar relativistic effects were included by means of the zero-order regular approximation,[88] while spin-orbit coupling (SOC) was further included in PBEsol0 calculations. Standard FHI-aims tier-2 basis sets were used in combination with a Γ-centered 4×4×4 *k*-point mesh. In the interest of open materials science,[32] all relevant DFT calculation data are publicly available from the Novel Materials Discovery (NOMAD) repository[89,90] via doi:10.17172/NOMAD/2021.09.15-1.

3. Results and Discussion

3.1. Octahedral-Tilting PESs

The surrogate models for the energy landscapes produced by 3D octahedral tilting provide insight into the energetics of disorder in $CsPbI_3$ and $CsPbBr_3$. We monitored the convergence of the models to ensure that the landscapes were well converged and reliable. **Figure 2**a,b illustrates important 2D cross sections of the 3D PES of $CsPbI_3$, which were constructed by merging the first 23, 75, 76, and 34 DFT calculations (809, 795, 797, and 793 symmetry-unfolded points) in the ppp, ppm, pmm, and mmm search spaces, respectively. The total-space database consists of 203 nonequivalent DFT calculations which are symmetrized into 982 data points. The 3D PES of $CsPbBr_3$ (Figure 2c,d) was fit to 195 DFT calculations (937 data points) collected from 38, 65, 70, and 27 DFT-calculated entries (815, 799, 797, and 793 data points) in ppp, ppm, pmm, and mmm, respectively. Some further 2D cross sections of the 3D PESs of both benchmark systems can be found in Section S3, Supporting Information.

At the outset, it is important to verify the quality of the PES surrogate models. The $a^+b^-b^-$ and $a^+b^-_mc^-$ cross sections of $CsPbI_3$ (Figure 2a-top and middle, respectively) agree with the previously reported 2D PESs of the same material very well.[20] We note that 76 DFT calculations sufficed to converge the 3D PES of pmm in our approach, while in ref. [20], 289 DFT data points sampled over an equispaced grid in a quadrant of the 2D configuration space supplied a 2D PES. This comparison demonstrates the validity, accuracy, and the remarkable efficiency of our 3D approach aided by BO.

The global minima (including symmetry-equivalent structures) in each search space are marked by white dots in Figure 2. Their structures are shown in **Figure 3** (further views of them are provided in Section S4, Supporting Information). **Table 2** features the tilting angle locations and PES values of

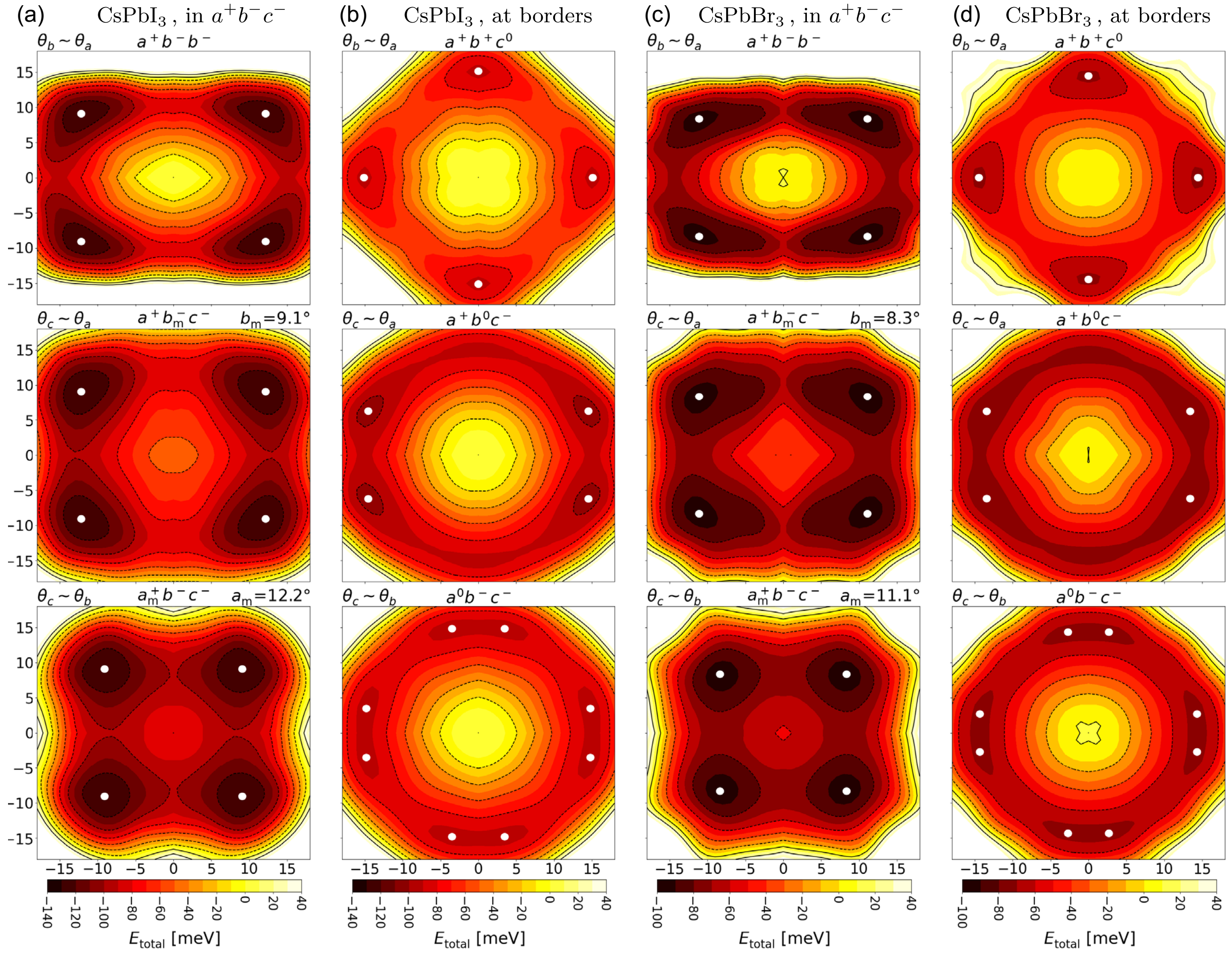

Figure 2. 2D cross sections of 3D PESs of a,b) $CsPbI_3$ and c,d) $CsPbBr_3$. Total energies, E_{total}, are given in their difference to the $a^0a^0a^0$ structure in meV per $CsPbX_3$ unit. For each material: (a,c) cross sections $a^+b^-b^-$, $a^+b^-_mc^-$, and $a^+_mb^-c^-$ within pmm (subscript "m" in the Glazer tilting notation means that the corresponding variable is kept constant at its value at the PES minimum), with white dots indicating the global E_{total} minima in the total space. (b,d) border planes $a^+b^+c^0$ (shared by ppp and ppm), $a^+b^0c^-$ (shared by ppm and pmm), and $a^0b^-c^-$ (shared by pmm and mmm), with white dots corresponding to the lowest energies in ppp, ppm, and mmm, respectively. The axis names of each plot are given at the top-left corner, for example, $\theta_b \approx \theta_a$ meaning θ_b and θ_a (both in °) for the vertical and horizontal axes, respectively. All figures have the same x and y scales. Note the different colormap scales for different materials.

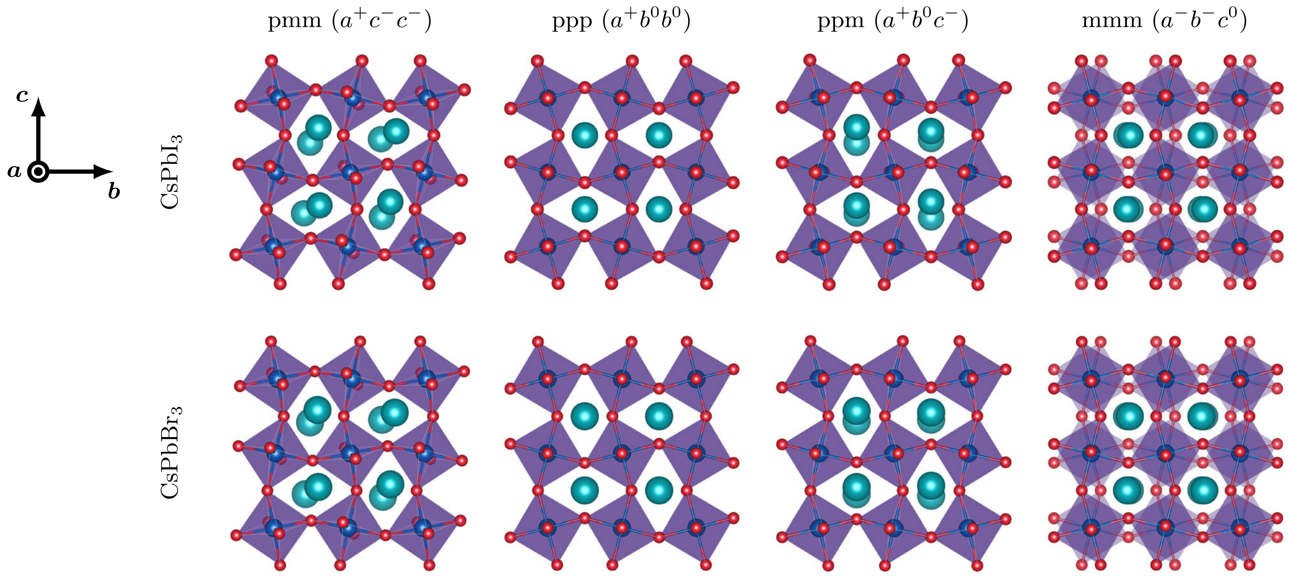

Figure 3. Structures of CsPbI$_3$ (upper panel) and CsPbBr$_3$ (lower panel) that correspond to the global minimum of each search space as indicated. Symmetry-equivalent structures are not shown. The Cs$^+$, Pb^{2+}, and halide (I$^-$ or Br$^-$) ions are colored in green, blue, and red, respectively. The octahedra are highlighted in purple. For each structure, the tilting around *a* has the largest amplitude (the approximate directions of lattice vectors *a*, *b*, and *c* are given).

Table 2. Structural data of global minima of all search spaces (the global minimum of the total space is marked by *). Positive and negative tilting angles (in °) indicate in-phase and out-of-phase tilts, respectively. E_{total} is the total energy evaluated based on the 3D PES surrogate models. Also listed are the total energy of corresponding structures fully relaxed with DFT ($E_{\text{f.r.}}$). Both energies are given in their difference to the $a^0a^0a^0$ structure in meV per CsPbX$_3$ unit.

Search space	*pmm*	ppp	ppm	mmm
CsPbI$_3$				
θ_a	12.2	15.1	14.5	−14.8
θ_b	−9.1	0	0	−3.5
θ_c	−9.1	0	−6.2	0
E_{total}	−129.2	−91.3	−103.5	−93.2
Space group	*Pnma*	*P*4/*mbm*	*Cmcm*	*C*2/*m*
$E_{\text{f.r.}}$	−132.6	−91.5	−104.1	−93.7
In Figure 2	a)	b)-$a^+b^+c^0$	(b)-$a^+b^0c^-$	b)-$a^0b^-c^-$
CsPbBr$_3$				
θ_a	11.1	14.4	13.4	−14.3
θ_b	−8.3	0	0	−2.7
θ_c	−8.3	0	−6.2	0
E_{total}	−93.9	−71.5	−77.5	−72.5
Space group	*Pnma*	*P*4/*mbm*	*Cmcm*	*C*2/*m*
$E_{\text{f.r.}}$	−97.3	−71.5	−78.3	−73.2
In Figure 2	c)	d)-$a^+b^+c^0$	d)-$a^+b^0c^-$	d)-$a^0b^-c^-$

all minima, as well the results of subsequent full structure relaxations. The total energies derived from the surrogate model (E_{total}) are only <3.5 meV per perovskite unit higher than the DFT full-relaxation results ($E_{\text{f.r.}}$), further confirming the accuracy of the 3D PES surrogate models. This difference is attributed to the constraint of the tilting patterns in DFT calculations. Since the difference is very small, we conclude that the three tilting angles are suitable principal DOFs.

The lowest-energy structures of both materials exhibit the $a^+b^-b^-$ tilting pattern (γ phase, space group *Pnma*) that is found in pmm (Figure 2a,c). The 2D cross sections of the 3D PESs in this space are qualitatively similar for these two materials. The main difference is that the global minimum of CsPbI$_3$ is lower than CsPbBr$_3$ by 35.3 meV per unit. In addition, the low-energy basins in CsPbBr$_3$ are less steep than in CsPbI$_3$. This can be rationalized by structural considerations: the Goldschmidt tolerance factor of CsPbBr$_3$ (0.862) is larger than that of CsPbI$_3$ (0.851) due to the smaller radius of the Br$^-$ anion. CsPbI$_3$ therefore has a stronger tendency toward octahedra tilting to stabilize its structure, resulting in more energy gained compared to the untilted structure and a steeper PES in the vicinity of the minimum.

Based on the 3D PES surrogate models, we can use the nudged elastic band method to easily evaluate the barrier of the MEPs that connect a global minimum and its symmetric image. The most important results are presented in **Table 3** (see Section S5, Supporting Information for more details). The smallest barriers are 25.7 and 16.4 meV for CsPbI$_3$ and CsPbBr$_3$, respectively, associated with the $a^+b^-b^- \rightarrow a^+b^-c^0 \rightarrow a^+b^-(-b)^-$ transition path. The lower barrier of CsPbBr$_3$ is a direct result of the shallower basin in the vicinity of the global minima. The MEPs linking $a^+b^-b^-$ and $(-a)^+b^-b^-$ have higher barriers, indicating that more energy is required to reverse the direction of an in-phase tilt than for an out-of-phase tilt. The transition $a^+b^-b^- \rightarrow a^+(-b)^-(-b)^-$ follows two consecutive MEPs, each associated with the direction reversal of an out-of-phase tilt.

Table 3. MEPs connecting the global-minimum structure $a^+b^-b^-$ and its symmetry equivalent structures and the associated barriers.

Structure-variation MEP	Barrier [meV]	
	$CsPbI_3$	$CsPbBr_3$
$a^+b^-b^- \rightarrow a^+b^-c^0 \rightarrow a^+b^-(-b)^-$	25.7	16.4
$a^+b^-b^- \rightarrow a^0b^-c^- \rightarrow (-a)^+b^-b^-$	35.9	
$a^+b^-b^- \rightarrow a^0b^-b^- \rightarrow (-a)^+b^-b^-$		23.1
$a^+b^-b^- \rightarrow a^+b^-c^0 \rightarrow a^+b^-(-b)^- \rightarrow a^+b^0(-c)^- \rightarrow a^+(-b)^-(-b)^-$	25.7	16.4

A simultaneous direction reversal of the two out-of-phase tilts is not favored. Our findings for $CsPbI_3$ that 1) the lowest barrier is associated with a transition-state structure with $a^+b^-c^0$ tilting and 2) its energy is lower than what is found in the 2D approach by a few meV (see Section S5, Supporting Information) are in good agreement with Klarbring's results.[20] The advantage of our BOSS approach is that we can directly evaluate the MEP within the 3D PES, so that we neither need to calculate several 2D PESs nor will miss the path with the lowest barrier.

The other three search spaces are naturally of less interest than pmm as they do not contain the overall most stable structure. For an in-depth insight into the tilting modes, we nevertheless briefly discuss them based on Figure 2b,d. Table 2 already indicates that the white dots in the top, middle, and bottom of Figure 2b,d are the global minima in the ppp, ppm, and mmm search spaces, respectively. The lowest-energy structure of ppp has $a^+b^0b^0$ tilting (space group $P4/mbm$), which is generally considered as the structure of the recently reported tetragonal β phase.[17,18,91] This structure is very localized in terms of the single in-phase tilting angle, which is obviously larger than the in-phase tilting angle of the overall most stable ($a^+b^-b^-$) structure (see Table 2). This structure also belongs to the ppm space group but is not the most stable one within this search space. The global minimum of ppm is instead located at $a^+b^0c^-$ whose energy is lower than the $a^+b^0b^0$ structure by 12.2 meV. It is the transition-state structure of the $a^+b^-b^- \rightarrow a^+(-b)^-b^-$ MEP. The local minimum of mmm exhibits $a^-b^-c^0$ tilting with one large (>10°) and one small (<5°) out-of-phase tilt. The barrier of the amplitude-exchange pathway, $a^0b^-c^- \rightarrow a^0c^-b^-$, is rather low (see Section S5, Supporting Information). Finally, none of the $a^-b^0b^0$ (space group $I4/mcm$) structures are a global minimum in any search space. This might explain why it has never been experimentally observed.

Summarizing Figure 2b,d provides insight into structural disorder in these two benchmark systems. The in-phase and out-of-phase tilts have different characters. An in-phase tilt around one lattice vector "excludes" in-phase tilts around any other lattice vectors, while an out-of-phase tilt can stabilize the structure with an in-phase tilt and can coexist and exchange energy with another out-of-phase tilt. We can thus conclude that the out-of-phase tilting mode is more active than the in-phase mode in $CsPbX_3$. The motion of out-of-phase tilts transfers vibrational energy from one lattice vector to another, giving rise to noticeable dynamical structural disorder.

3.2. Configuration Space Distribution of Structures at Finite Temperatures

Based on the total-energy profiles in the 3D configuration space, we can analyze the distribution of the structural disorder of $CsPbI_3$ and $CsPbBr_3$ at finite temperatures. **Figure 4** sketches the total energy data listed in Table 2 and facilitates the prediction of how structures evolve and disorder grows in both systems with increasing temperature.

From the BOSS surrogate PES model (Figure 2), we calculated the probability density of finding $CsPbI_3$ or $CsPbBr_3$ in a structure that is labeled by point $\boldsymbol{\theta}$ (a shortened notation of tilting angles) in the total configuration space at temperature T using the Boltzmann distribution

$$\rho(\boldsymbol{\theta}, T) \propto \mathrm{e}^{-[E(\boldsymbol{\theta})-E_{\min}]/k_B T} \tag{1}$$

Here $E(\boldsymbol{\theta})$ and $E_{\min}$ denote the energies of structure $\boldsymbol{\theta}$ and the overall most stable structure, respectively. k_B is the Boltzmann constant. In this work, we have not normalized the total probability but rather kept the maximum probability density always at 1. We can thus set a criterion of ρ (0.5 in this work) to help investigate the distribution of thermal population of disordered structures. We are especially interested in two features: 1) the region within which $\rho > 0.5$ (the larger the region, the more extensive the disorder) and 2) whether the $\rho > 0.5$ distribution emerges at some particular regions in the configuration space (meaning noticeable population at the corresponding tilting patterns). Representative results are illustrated in **Figure 5** (see also Section S6, Supporting Information).

Figure 5a shows that $CsPbI_3$ is quite strongly bound in its most stable $a^+b^-b^-$ ($Pnma$, γ phase) structure at 300 K. As temperature increases, the $\rho > 0.5$ regions grow gradually and reach the $a^+b^-c^0$ plane first at 450 K (Figure 5b). This corresponds to the A → B transition in Figure 4, which requires an energy of 25.7 meV. At this point, the structure has not yet gained enough energy to further travel across a series of $a^+b^+c^-$ structures (B → C in Figure 4), but will rather be "reflected" by this $a^+b^-c^0$ border back to pmm. It can either go back to the initial $a^+b^-b^-$ structure or fall into another equivalent $a^+b^-(-b)^-$ minimum with the

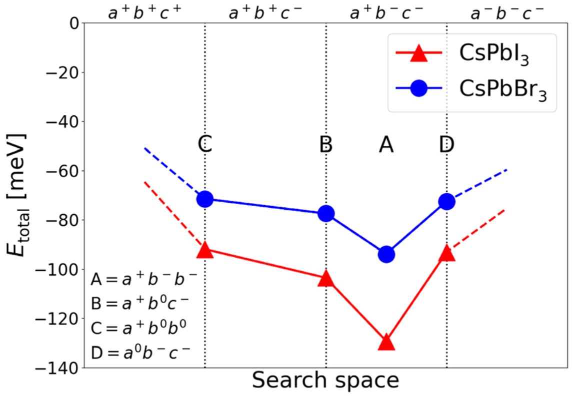

Figure 4. Energies of the most stable structures (labeled by A–D) in the four search spaces (red triangles and blue circles for $CsPbI_3$ and $CsPbBr_3$, respectively).

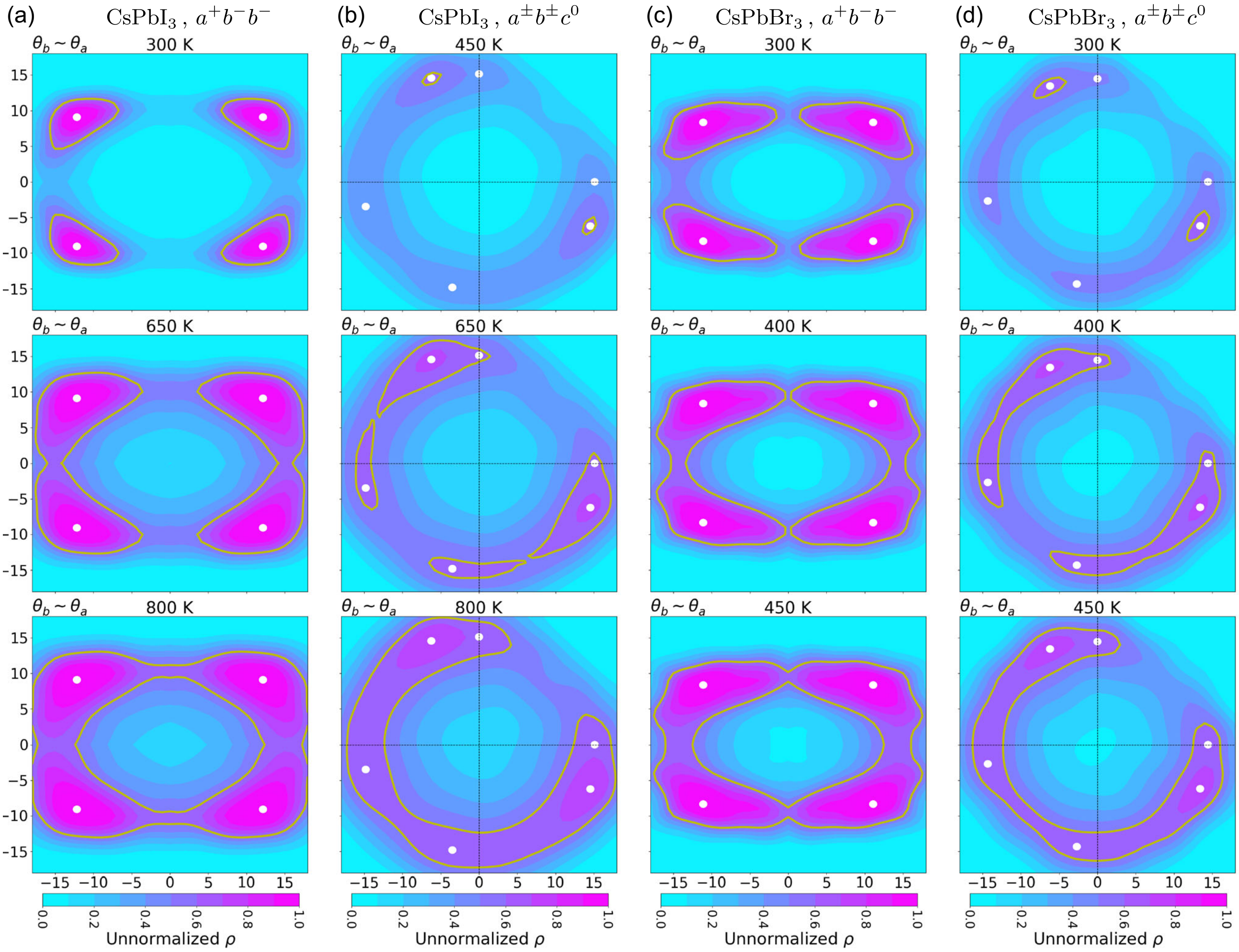

Figure 5. 2D cross sections of unnormalized distribution probability density of a,b) $\mathrm{CsPbI_3}$ and c,d) $\mathrm{CsPbBr_3}$ in the search spaces of tilting angles at different temperatures. Shown for each material: (a,c) $a^+b^-b^-$ cross section from pmm and (b,d) $a^\pm b^\pm c^0$ cross section from the total configuration space. The thick yellow lines in each plot mark a relative probability of 0.5.

direction of one out-of-phase tilt reversed around the lattice vector. Our observation of the $a^+b^-b^- \rightarrow a^+b^-c^0 \rightarrow a^+b^-(-b)^-$ mechanism is in good agreement with the previous study of the structural disorder for the observed β-$\mathrm{CsPbI_3}$ by Klarbring.[20]

As temperature further increases beyond 450 K, a noticeable population of $\mathrm{CsPbI_3}$ structures at $a^+b^0b^0$ (Figure 5a) and $a^-b^-c^0$ (Figure 5b) is observed at 650 K. The former corresponds to "C" in Figure 4, with only one single in-phase tilt while both out-of-phase tilts are largely suppressed. The latter corresponds to "D" in Figure 4. The structure can easily fluctuate between in-phase and out-of-phase tilts at this temperature, too. The direction reversal of the in-phase tilt, $a^+ \rightarrow (-a)^+$, becomes highly probable at 800 K. The motion of the less active in-phase tilt gives rise to an extremely high level of structural disorder.

$\mathrm{CsPbBr_3}$ exhibits generally similar features (Figure 5c,d), yet noticeable differences can be observed. Because of the shallower PES basins, the probability distribution of $\mathrm{CsPbBr_3}$ at 300 K is much broader than $\mathrm{CsPbI_3}$. First, $\rho > 0.5$ can already be observed at $a^+b^-c^0$ at room temperature due to a much lower activation energy (16.4 meV). At 400 K, the $a^+b^0b^0$ ($P4/mbm$) structure is populated. At this temperature, we also observe $a^+b^0 \leftrightarrow a^0b^-$ tilting-mode transitions. Finally, at 450 K the $a^+ \leftrightarrow (-a)^+$ motion sets in. All of these findings indicate a much more disordered structure in $\mathrm{CsPbBr_3}$ than its iodide analog at the same temperature.

Table 4 summarizes the important phenomena derived from Figure 5 and S3, Supporting Information. Both benchmark systems exhibit a three-stage mechanism of structure variation as temperature increases. Starting from the most stable $a^+b^-b^-$ structure, we can first observe the motion of one out-of-phase tilting mode, $a^+b^-b^- \leftrightarrow a^+b^-c^0$. This process is closely related to the γ → β phase transition. In our work, the temperature of this stage is very close to the phase-transition temperature for $\mathrm{CsPbI_3}$ (450 vs. 448 K[17,18]) but clearly lower than that for $\mathrm{CsPbBr_3}$ (300 vs. 361 K[69,92]). A further temperature increase activates the motion of another out-of-phase tilt and the fluctuation between the out-of-phase and in-phase tilts. Finally, direction reversal of any mode and switch between any two modes become prevalent, giving rise to the highly disordered, effectively

Table 4. Important tilting patterns: the (approximate) temperature at which they become noticeably populated, and the tilting-mode transition to which they closely correspond.

Tilting pattern	Relevant transition of tilting modes	T of emergence [K]	
		$CsPbI_3$	$CsPbBr_3$
$a^+b^-c^0$	$a^+b^-b^- \rightarrow a^+b^-(-b)^-$	450	<300
$a^+b^0b^0$	$a^+b^-c^0 \rightarrow a^+(-b)^-c^0$	650	400
$a^-b^0b^0$	$a^+b^0b^0 \rightarrow a^0b^-a^0$	650	400
$a^-a^-c^0$	$a^-b^0b^0 \rightarrow a^0b^-a^0$	800	450

cubic structure with pronounced lattice vibrations. In our work the temperature of this stage is a bit higher than the β→α phase-transition temperature for $CsPbBr_3$ (450 vs. 403 K[69,92]) and much higher than that for $CsPbI_3$ (800 vs. 533 K[17,18]). Our calculations do not include entropy contributions and can therefore not be expected to provide a close match to experimental transition temperatures. The focus of this work is to understand the nature of structural disorder of these emergent and important optoelectronic materials at the atomic scale. The PES database created in this article has laid a solid groundwork for the direct simulation of the γ→β→α phase transition, which is beyond the scope of this work.

As a concluding note, we emphasize that the zero-tilting structure $a^0a^0a^0$, which is generally regarded as the α (cubic) phase, is very rarely populated even at >800 K. This is simply because it is energetically much less favorable than the most stable $a^+b^-b^-$ structure. Our results indicate that the cubic phase must be understood as a dynamic average of disordered lower-symmetry structures, a result that was found by a recent DFT and molecular dynamics study for $CsPbBr_3$.[24] In this phase, plenty of domains or nanoregions of low-symmetry structures (such as $a^+b^-b^-$) occur with equal probability; the octahedra of each nanoregion are dynamically fluctuating to adapt to their neighbors, thus giving rise to an effectively cubic average structure.

3.3. Bandgap Distributed Over Disordered Structures

With the sampled DFT calculations we are able to fit surrogate models for materials properties of interest other than PESs. The bandgap is one of the most important electronic structure properties for optoelectronic materials. Here we focus on how bandgaps of the benchmark systems vary with octahedral-tilting angles.

Figure 6 provides representative 2D cross sections of 3D surrogate models that are fitted to the bandgap data calculated with DFT (PBEsol0+SOC). For $CsPbI_3$, we observe that the bandgap increases monotonically with tilting angle. While for $CsPbBr_3$ the

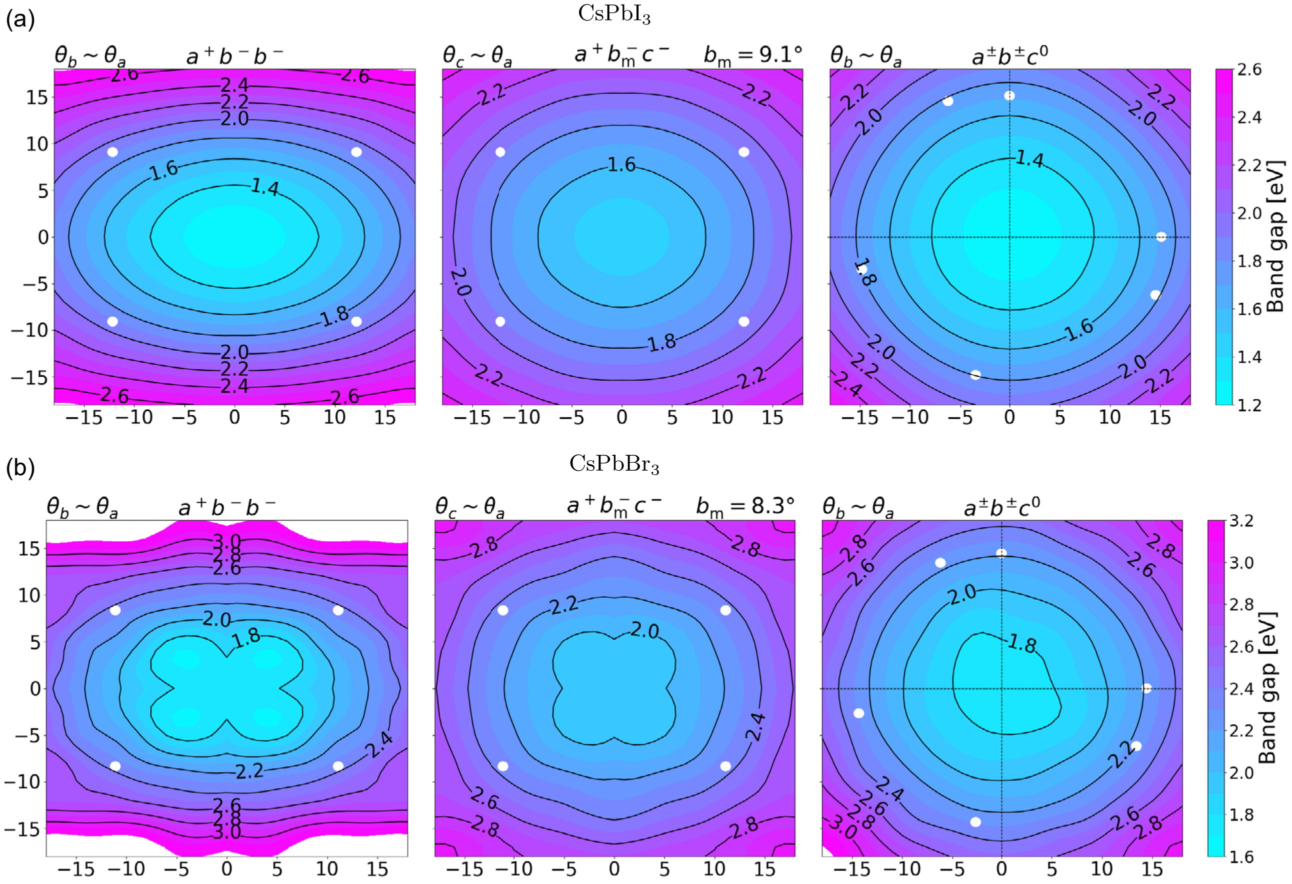

Figure 6. Bandgaps of a) $CsPbI_3$ and b) $CsPbBr_3$ in the search space of tilting angles (shown are 2D cross sections $a^+b^-b^-$, $a^+b_m^-c^-$, and $a^{\pm}b^{\pm}c^0$ of the 3D surrogate models).

overall trend is the same, small deviations are observed when all three tilting angles are small.

It it noteworthy that the cubic $a^0a^0a^0$ structure has an obviously lower bandgap than all minima structures in different search spaces (white dots in Figure 6) for each benchmark system. This is due to the maximal overlap of atomic orbitals as a result of the zero tilt, which broadens the valence and conduction bands, thus reducing the gap. As already alluded to, such a cubic structure is not seen in experiments, because it is too high in energy. The experimental bandgaps of $CsPbI_3$ and $CsPbBr_3$ are ≈1.7[17,93,94] and ≈2.3 eV,[69,95] respectively. DFT bandgaps of all minima structures fall into those regions (see also Section S7, Supporting Information), indicating that the PBEsol0+SOC approach with $\alpha = 0.25$ is a suitable choice for both materials.

Based on the bandgap surrogate model, we calculated the temperature-dependent average bandgap of each system by

$$\langle E_{\mathrm{gap}}(T)\rangle = \frac{\int \rho(\boldsymbol{\theta},T)E_{\mathrm{gap}}(\boldsymbol{\theta})d\boldsymbol{\theta}}{\int \rho(\boldsymbol{\theta},T)d\boldsymbol{\theta}} \tag{2}$$

where the integrations run over the whole configuration space, $E_{\mathrm{gap}}(\boldsymbol{\theta})$ is the BOSS-predicted bandgap at $\boldsymbol{\theta}$, and the weighting factor $\rho(\boldsymbol{\theta},T)$ is the distribution density displayed in Figure 5. Results are illustrated in the left column of **Figure 7**. The right column of Figure 7 displays the search space-resolved bandgap versus total energy relationship based on the BOSS surrogate model data.

At 0 K, both systems are in their $a^+b^-b^-$ global-minimum structures (with some small-amplitude zero-point vibrations). The calculated bandgaps are accordingly 1.90 and 2.33 eV for $CsPbI_3$ and $CsPbBr_3$, respectively. As temperature increases, structural disorder grows first mainly within pmm (blue in Figure 7-right). The average bandgap decreases as the contribution of ppm (green) increases, since the bandgaps of ppm structures within the low-energy range are generally smaller than pmm. A further temperature increase enlarges the contribution from both mmm and ppp to the average bandgap. The band gap range of mmm (red) is above ppp (yellow). For $CsPbI_3$ (Figure 7a), the bandgap range of the union of mmm and ppp approximately superposes ppm. Consequently, the average bandgap stabilizes between 300 and 700 K (1.81 and 1.82 eV,

(a) $CsPbI_3$

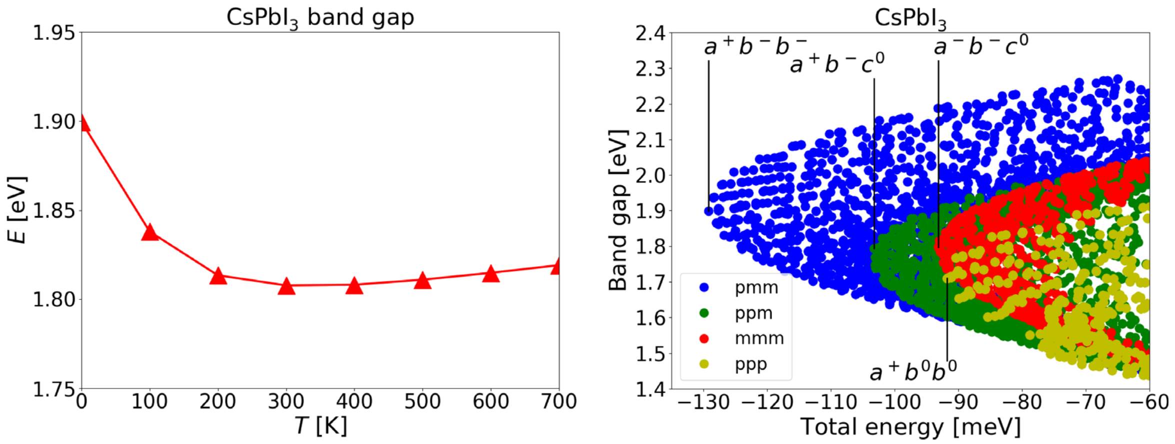

(b) $CsPbBr_3$

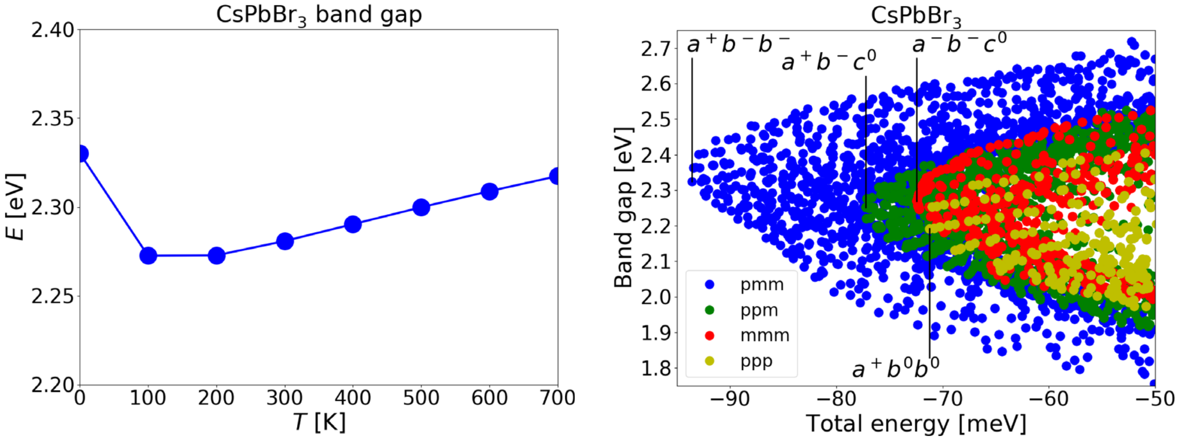

Figure 7. Temperature dependence of the average bandgaps (left) and the bandgap versus total-energy relationship (right) of a) $CsPbI_3$ and b) $CsPbBr_3$. In the right plots, only the BOSS surrogate-model data within the low-energy range are shown. Data from pmm, ppm, mmm, and ppp are colored in blue, green, red, and yellow, respectively. The tilting pattern of the data entry corresponding to the local minimum of each tilting-pattern category is highlighted.

respectively). While for $CsPbBr_3$ (Figure 7b) at $T > 300$ K, the bandgap range of mmm⊕ppp is slightly higher than ppm, thus resulting in a slowly increasing average bandgap with temperature (2.28 and 2.32 eV at 300 and 700 K, respectively).

Figure 8 shows the band structures and densities of states of some tilted pmm structures. For $CsPbI_3$, the total energies of the structures in Figure 8a,b are close to that of the minimum ppm structure ($a^+b^-c^0$, −103.5 meV). The bandgap of the pmm

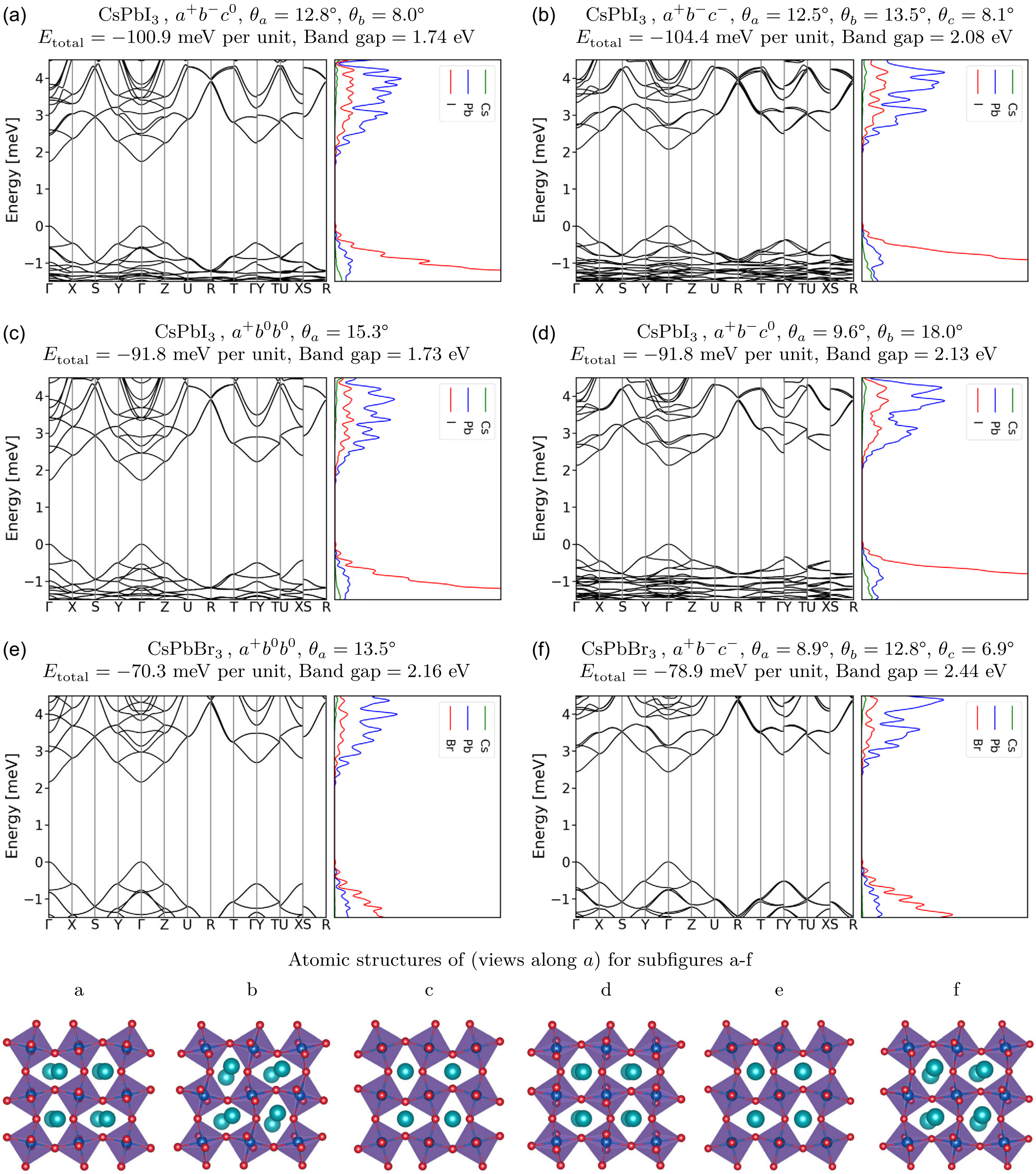

Figure 8. Band structures and densities of states of some disordered a–d) $CsPbI_3$ and e–f) $CsPbBr_3$ structures. Also shown are their atomic structure (view along lattice vector ***a***). We arrive at the high-symmetry point labels in the band structures by treating the 2×2×2 model as quasiorthorhombic with equal lattice constants. Contributions from Cs, Pb, and halide atoms to the partial density of states are colored in green, blue, and red, respectively.

minimum structure (1.91 eV) lies in between those of structures a (1.74 eV) and b (2.08 eV). A similar behavior can be observed for the structures in Figure 8c,d, whose total energies are close to the minima of mmm ($a^-b^-c^0$, −93.2 meV) and ppp ($a^+b^0b^0$, −91.5 meV). For $CsPbBr_3$ we only show two structures (Figure 8e,f), whose energies are in the range of [−80, −70] meV where also the ppm, mmm, and ppp minima can be found. Compared to the pmm minimum structures of both compounds (parameters cf. Table 2), the structures with smaller bandgaps (Figure 8a,c,e) exhibit smaller out-of-phase tilting angles, while in the structures with larger bandgaps (Figure 8b,d,f), one of the out-of-phase tilts exhibits an angle larger than the in-phase tilt. Section S8, Supporting Information, provides the electronic structure of minimum structures in all four search spaces as well as the untilted cubic structure for both compounds.

For $CsPbBr_3$, the calculated average bandgap at room temperature or above agrees well with experiments (ranging between 2.25[69] and 2.39 eV[95]). Our data reproduce the experimentally observed trend that the bandgap increases with temperature above 300 K.[95] For $CsPbI_3$, our model somehow overestimates the bandgap (reported experimental bandgaps are 1.67 eV for the γ phase[17] and 1.73 eV for the α phase[93,94]). The accuracy of bandgap estimation certainly depends on the computational settings (e.g., the amount of exact exchange in a hybrid functional), for which we need benchmark studies in the future. In addition, we note that our calculations were conducted for $2 \times 2 \times 2$ model systems. For very large models, disorder-induced wavefunction localization will occur, therewith statistical effects will emerge and have impact on the bandgap calculations. This is beyond the scope of this work.

Based on our full-dimensional PESs, we can already propose valuable strategies to design next-generation optoelectronic materials. For example, smaller tilting angles are desired to tune the bandgap of photovoltaic material $CsPbI_3$ to the optimal ≈1.35 eV according to the Shockley–Queisser theory.[96] Doping with organic monovalent A-site cations that are larger than Cs^+ would be a solution. While for $CsPbBr_3$ in green-light emission, we are interested in materials with minimal structural disorder for high monochromaticity. A-site mixing with cations smaller than Cs^+ and X-site mixing with larger anions would be promising options.

4. Conclusion

This work offers new computational insights into the structural disorder in benchmark systems $CsPbI_3$ and $CsPbBr_3$. With relatively few first-principles (DFT) calculations sampled with the BOSS scheme, we have obtained accurate landscapes for both total energy and bandgap, each as a function of octahedral-tilting angles. We could infer how the distribution of crystal structures evolves within the 3D octahedral-tilting configuration space with increasing temperature. We then evaluated the statistical mean of bandgap, an important materials property for optoelectronic application, over the disordered structures. Our work demonstrates that novel cross-disciplinary ML computational materials science tools such as BOSS can aid the description of structural disorder phenomena, which is important to make recommendation for rational design of advanced functional materials such as halide perovskites.

Supporting Information

Supporting Information is available from the Wiley Online Library or from the author.

Acknowledgements

The authors thank Jari Järvi, Joakim Löfgren, Jarno Laakso, Azimatu Fangnon, Zhaoxin Wu, and Nan Zhang for the fruitful discussions. The authors acknowledge the computing resources by Xi'an Jiaotong University's HPC platform, the Hefei Advanced Computing Center, the Aalto Science-IT project, and the CSC-IT Center for Science. This work was supported by the Natural Science Foundation of Shaanxi Province of China (grant no. 2023-YBGY-447), National Natural Science Foundation of China under grant nos. 62281330043, 11974268, 21503057, 12111530061, and 5237212, the Fundamental Research Funds for the Central Universities (grant nos. HIT.NSRIF.2017032 and xzy012021025), the China Postdoctoral Science Foundation (grant no. 2018M643632), the Natural Sciences & Engineering Research Council of Canada (NSERC, grant no. RGPIN-2017-06915), the European Union's Horizon 2020 research and innovation program under grant agreement no. 676580 [The Novel Materials Discovery (NOMAD)], and the Academy of Finland (grant nos. 316601, 334532, and 305632).

Conflict of Interest

The authors declare no conflict of interest.

Data Availability Statement

The data that support the findings of this study are openly available in [NOMAD (Novel Materials Discovery)] at [https://doi.org/10.17172/NOMAD/2021.09.15-1], reference number [0].

Keywords

Bayesian optimizations, cesium lead halide perovskites, first-principles calculations, multidimensional potential-energy surfaces, structural disorders

Received: May 28, 2024
Revised: June 22, 2024

---

[1] P. K. Nayak, G. Garcia-Belmonte, A. Kahn, J. Bisquert, D. Cahen, *Energy Environ. Sci.* **2012**, *5*, 6022.
[2] A. B. Cairns, A. L. Goodwin, *Chem. Soc. Rev.* **2013**, *42*, 4881.
[3] D. A. Keen, A. L. Goodwin, *Nature* **2015**, *521*, 303.
[4] D. Rhodes, S. H. Chae, R. Ribeiro-Palau, J. Hone, *Nat. Mater.* **2019**, *18*, 541.
[5] N. Dragoe, D. Bérardan, *Science* **2019**, *366*, 573.
[6] V. L. Deringer, *J. Phys. Energy* **2020**, *2*, 041003.
[7] A. Simonov, A. L. Goodwin, *Nat. Rev. Chem.* **2020**, *4*, 657.
[8] V. L. Deringer, N. Bernstein, G. Csányi, C. Ben Mahmoud, M. Ceriotti, M. Wilson, D. A. Drabold, S. R. Elliott, *Nature* **2021**, *589*, 59.
[9] Z.-G. Ye, *MRS Bull.* **2009**, *34*, 277.
[10] S. Zhang, F. Li, X. Jiang, J. Kim, J. Luo, X. Geng, *Prog. Mater. Sci.* **2015**, *68*, 1.
[11] E. Sun, W. Cao, *Prog. Mater. Sci.* **2014**, *65*, 124.

[12] M. Abdi-Jalebi, Z. Andaji-Garmaroudi, A. J. Pearson, G. Divitini, S. Cacovich, B. Philippe, H. Rensmo, C. Ducati, R. H. Friend, S. D. Stranks, *ACS Energy Lett.* **2018**, *3*, 2671.
[13] J.-P. Correa-Baena, T. M. Brenner, J. Snaider, S. Sun, X. Li, M. A. Jensen, N. T. P. Hartono, L. Nienhaus, S. Wieghold, J. R. Poindexter, S. Wang, Y. S. Meng, T. Wang, B. Lai, M. V. Holt, Z. Cai, M. G. Bawendi, L. Huang, T. Buonassisi, D. P. Fenning, *Science* **2019**, *363*, 627.
[14] D. Shin, B. Saparov, D. B. Mitzi, *Adv. Energy Mater.* **2017**, *7*, 1602366.
[15] S. Giraldo, Z. Jehl, M. Placidi, V. Izquierdo-Roca, A. Pérez-Rodríguez, E. Saucedo, *Adv. Mater.* **2019**, *31*, 1806692.
[16] S. Tan, B. Yu, Y. Cui, F. Meng, C. Huang, Y. Li, Z. Chen, H. Wu, J. Shi, Y. Luo, D. Li, Q. Meng, *Angew. Chem., Int. Ed.* **2022**, *61*, e202201300.
[17] C. C. Stoumpos, M. G. Kanatzidis, *Acc. Chem. Res.* **2015**, *48*, 2791.
[18] A. Marronnier, G. Roma, S. Boyer-Richard, L. Pedesseau, J.-M. Jancu, Y. Bonnassieux, C. Katan, C. C. Stoumpos, M. G. Kanatzidis, J. Even, *ACS Nano* **2018**, *12*, 3477.
[19] R. Jinnouchi, J. Lahnsteiner, F. Karsai, G. Kresse, M. Bokdam, *Phys. Rev. Lett.* **2019**, *122*, 225701.
[20] J. Klarbring, *Phys. Rev. B* **2019**, *949*, 104105.
[21] L. Chen, B. Xu, Y. Yang, L. Bellaiche, *Adv. Funct. Mater.* **2020**, *30*, 1909496.
[22] C. E. Patrick, K. W. Jacobsen, K. S. Thygesen, *Phys. Rev. B* **2015**, *92*, 201205.
[23] R. X. Yang, J. M. Skelton, E. L. da Silva, J. M. Frost, A. Walsh, *J. Phys. Chem. Lett.* **2020**, *152*, 024703.
[24] X. Zhu, S. Caicedo-Dávila, C. Gehrmann, D. A. Egger, *ACS Appl. Mater. Interfaces* **2022**, *14*, 22973.
[25] S. Kirkpatrick, C. G. Gellatt, M. P. Vecchi, *Science* **1983**, *220*, 671.
[26] S. Goedecker, W. Hellmann, T. Lenosky, *Phys. Rev. Lett.* **2005**, *95*, 055501.
[27] R. O. Jones, *Rev. Mod. Phys.* **2015**, *87*, 897.
[28] R. H. Bisseling, R. Kosloff, D. Kosloff, *Comput. Phys. Commun.* **1986**, *39*, 313.
[29] T. Wu, H.-J. Werner, U. Manthe, *Science* **2004**, *306*, 2227.
[30] G. R. Schleder, A. C. M. Padilha, C. Mera Acosta, M. Costa, A. Fazzio, *J. Phys.: Mater.* **2019**, *2*, 032001.
[31] J. Schmidt, M. R. G. Marques, S. Botti, M. A. L. Marques, *npj Comput. Mater.* **2019**, *5*, 83.
[32] L. Himanen, A. Geurts, A. S. Foster, P. Rinke, *Adv. Sci.* **2019**, *6*, 1900808.
[33] V. L. Deringer, M. A. Caro, G. Csányi, *Adv. Mater.* **2019**, *31*, 1902765.
[34] G. L. W. Hart, T. Mueller, C. Toher, S. Curtarolo, *Nat. Rev. Mater.* **2021**, *6*, 730.
[35] A. P. Bartók, M. C. Payne, R. Kondor, G. Csányi, *Phys. Rev. Lett.* **2010**, *104*, 136403.
[36] J. Behler, *J. Phys.: Condens. Matter* **2014**, *26*, 183001.
[37] M. d'Avezac, A. Zunger, *Phys. Rev. B* **2008**, *78*, 064102.
[38] Y. Wang, J. Lv, L. Zhu, Y. Ma, *Comput. Phys. Commun.* **2012**, *183*, 2063.
[39] S. Bhattacharya, S. V. Levchenko, L. M. Ghiringhelli, M. Scheffler, *Phys. Rev. Lett.* **2013**, *111*, 135501.
[40] T. Yamashita, N. Sato, H. Kino, T. Miyake, K. Tsuda, T. Oguchi, *Phys. Rev. Mater.* **2018**, *2*, 013803.
[41] M. S. Jørgensen, U. F. Larsen, K. W. Jacobsen, B. Hammer, *J. Phys. Chem. A* **2018**, *122*, 1504.
[42] M. K. Bisbo, B. Hammer, *Phys. Rev. Lett.* **2020**, *124*, 086102.
[43] H. L. Mortensen, S. A. Meldgaard, M. K. Bisbo, M.-P. V. Christiansen, B. Hammer, *Phys. Rev. B* **2020**, *102*, 075427.
[44] S. Kaappa, E. G. del Ro, K. W. Jacobsen, *Phys. Rev. B* **2021**, *103*, 174114.
[45] R. Wanzenböck, A. Marco, B. Sebastian, B. Florian, J. Carrete, G. K. H. Madsen, *Digital Discovery* **2022**, *1*, 703.
[46] M. Rupp, A. Tkatchenko, K.-R. Müller, O. A. von Lilienfeld, *Phys. Rev. Lett.* **2012**, *108*, 058301.
[47] V. Botu, R. Batra, J. Chapman, R. Ramprasad, *J. Phys. Chem. C* **2017**, *121*, 511.
[48] O. A. von Lilienfeld, K. Burke, *Nat. Commun.* **2020**, *11*, 4895.
[49] H. E. Sauceda, S. Chmiela, I. Poltavsky, K.-R. Müller, A. Tkatchenko, in *Machine Learning Meets Quantum Physics*, Vol. *277* (Eds: K. T. Schütt, S. Chmiela, O. A. von Lilienfeld, A. Tkatchenko, K. Tsuda, K.-R. Müller), Springer International Publishing, Cham **2020**.
[50] J. Vandermause, S. B. Torrisi, S. Batzner, Y. Xie, L. Sun, A. M. Kolpak, B. Kozinsky, *npj Comput. Mater.* **2020**, *6*, 20.
[51] J. Timmermann, Y. Lee, C. G. Staacke, J. T. Margraf, C. Scheurer, K. Reuter, *J. Chem. Phys.* **2021**, *155*, 244107.
[52] O. T. Unke, S. Chmiela, H. E. Sauceda, M. Gastegger, I. Poltavsky, K. T. Schütt, A. Tkatchenko, K.-R. Müller, *Chem. Rev.* **2021**, *121*, 10142.
[53] J. Westermayr, S. Chaudhuri, A. Jeindl, O. T. Hofmann, R. J. Maurer, *Digital Discovery* **2022**, *1*, 463.
[54] M. Todorovic, M. U. Gutmann, J. Corander, P. Rinke, *npj Comput. Mater.* **2019**, *5*, 35.
[55] L. Fang, E. Makkonen, M. Todorovc, P. Rinke, X. Chen, *J. Chem. Theory Comput.* **2021**, *17*, 1955.
[56] A. T. Egger, L. Hörmann, A. Jeindl, M. Scherbela, V. Obersteiner, M. Todorovic, P. Rinke, O. T. Hofmann, *Adv. Sci.* **2020**, *7*, 2000992.
[57] J. Järvi, P. Rinke, M. Todorovic, *Beilstein J. Nanotechnol.* **2020**, *11*, 1577.
[58] J. Järvi, B. Alldritt, O. Krejčí, M. Todorovic, P. Liljeroth, P. Rinke, *Adv. Funct. Mater.* **2020**, *31*, 2010853.
[59] A. Fangnon, M. Dvorak, V. Havu, M. Todorovic, J. Li, P. Rinke, *ACS Appl. Mater. Interfaces* **2022**, *14*, 12758.
[60] J. Chen, H. Dong, J. Li, X. Zhu, J. Xu, F. Pan, R. Xu, J. Xi, B. Jiao, X. Hou, K. W. Ng, S.-P. Wang, Z. Wu, *ACS Energy Lett.* **2022**, *7*, 3685.
[61] C. Zhang, Q. Liao, J. Chen, B. Li, C. Xu, K. Wei, G. Du, Y. Wang, D. Liu, J. Deng, Z. Luo, S. Pang, Y. Yang, J. Li, L. Yang, X. Guo, J. Zhang, *Adv. Mater.* **2023**, *35*, 2209422.
[62] A. Stuke, P. Rinke, M. Todorovic, *Mach. Learn.: Sci. Technol.* **2021**, *2*, 035022.
[63] J. Laakso, M. Todorovic, J. Li, G.-X. Zhang, P. Rinke, *Phys. Rev. Mater.* **2022**, *6*, 113801.
[64] S. Sun, A. Tiihonen, F. Oviedo, Z. Liu, J. Thapa, Y. Zhao, N. T. P. Hartono, A. Goyal, T. Heumueller, C. Batali, A. Encinas, J. J. Yoo, R. Li, Z. Ren, I. M. Peters, C. J. Brabec, M. G. Bawendi, V. Stevanovic, J. Fisher III, T. Buonassisi, *Matter* **2021**, *4*, 1305.
[65] J. Löfgren, D. Tarasov, T. Koitto, P. Rinke, M. Balakshin, M. Todorovic, *ACS Sustainable Chem. Eng.* **2022**, *10*, 9469.
[66] K. Sim, T. Jun, J. Bang, H. Kamioka, J. Kim, H. Hiramatsu, H. Hosono, *Appl. Phys. Rev.* **2019**, *6*, 031402.
[67] A. M. Glazer, *Acta Crystallogr.* **1972**, *B28*, 3384.
[68] I. Chung, J.-H. Song, J. Im, J. Androulakis, C. D. Malliakas, H. Li, A. J. Freeman, J. T. Kenney, M. G. Kanatzidis, *J. Am. Chem. Soc.* **2012**, *134*, 8579.
[69] C. C. Stoumpos, C. D. Malliakas, J. A. Peters, Z. Liu, M. Sebastian, J. Im, T. C. Chasapis, A. C. Wibowo, D. Y. Chung, A. J. Freeman, B. W. Wessels, M. G. Kanatzidis, *Cryst. Growth Des.* **2013**, *13*, 2722.
[70] C. Gehrmann, D. A. Egger, *Nat. Commun.* **2019**, *10*, 3141.
[71] A. M. Glazer, *Acta Crystallogr.* **1975**, *A31*, 756.
[72] P. M. Woodward, *Acta Crystallogr.* **1997**, *B53*, 32.
[73] P. M. Woodward, *Acta Crystallogr.* **1997**, *B53*, 44.
[74] M. A. Islam, J. M. Rondinelli, J. E. Spanier, *J. Phys.: Condens. Matter* **2013**, *25*, 175902.
[75] N. Xie, J. Zhang, S. Raza, N. Zhang, X. Chen, D. Wang, *J. Phys.: Condens. Matter* **2020**, *32*, 315901.

[76] C. E. Rasmussen, C. K. I. Williams, *Gaussian Processes for Machine Learning*, The MIT Press, Cambridge, MA **2006**.
[77] M. U. Gutmann, J. Corander, *J. Mach. Learn. Res.* **2016**, *17*, 1.
[78] E. Brochu, V. M. Cora, N. de Freitas, *arXiv:1012.2599*, **2010**.
[79] J. P. Perdew, A. Ruzsinszky, G. I. Csonka, O. A. Vydrov, G. E. Scuseria, L. A. Constantin, X. Zhou, K. Burke, *Phys. Rev. Lett.* **2008**, *100*, 136406.
[80] F. Knuth, C. Carbogno, V. Atalla, V. Blum, M. Scheffler, *Comput. Phys. Commun.* **2015**, *190*, 33.
[81] V. Blum, R. Gehrke, F. Hanke, P. Havu, V. Havu, X. Ren, K. Reuter, M. Scheffler, *Comput. Phys. Commun.* **2009**, *180*, 2175.
[82] V. Havu, V. Blum, P. Havu, M. Scheffler, *J. Comput. Phys.* **2009**, *228*, 8367.
[83] X. Ren, P. Rinke, V. Blum, J. Wieferink, A. Tkatchenko, A. Sanfilippo, K. Reuter, M. Scheffler, *New J. Phys.* **2012**, *14*, 053020.
[84] S. V. Levchenko, X. Ren, J. Wieferink, R. Johanni, P. Rinke, V. Blum, M. Scheffler, *Comput. Phys. Commun.* **2015**, *192*, 60.
[85] R. X. Yang, J. M. Skelton, E. L. da Silva, J. M. Frost, A. Walsh, *J. Phys. Chem. Lett.* **2017**, *8*, 4720.
[86] M. Bokdam, J. Lahnsteiner, B. Ramberger, T. Schäfer, G. Kresse, *Phys. Rev. Lett.* **2017**, *119*, 145501.
[87] A. Seidu, M. Dvorak, P. Rinke, J. Li, *J. Chem. Phys.* **2021**, *154*, 074712.
[88] E. van Lenthe, E. J. Baerends, J. G. Sneijders, *J. Chem. Phys.* **1993**, *99*, 4597.
[89] L. M. Ghiringhelli, C. Carbogno, S. Levchenko, F. Mohamed, G. Huhs, M. Lüders, M. Oliveira, M. Scheffler, *npj Comput. Mater.* **2017**, *3*, 46.
[90] C. Draxl, M. Scheffler, *MRS Bull.* **2018**, *43*, 676.
[91] Y. Wang, M. Ibrahim Dar, L. K. Ono, T. Zhang, M. Kan, Y. Li, L. Zhang, X. Wang, Y. Yang, X. Gao, Y. Qi, M. Grätzel, Y. Zhao, *Science* **2019**, *365*, 591.
[92] S. Hirotsu, J. Harada, M. Iizumi, K. Gesi, *J. Phys. Soc. Jpn.* **2013**, *37*, 1393.
[93] G. E. Eperon, S. D. Stranks, C. Menelaou, M. B. Johnston, L. M. Herz, H. J. Snaith, *Energy Environ. Sci.* **2014**, *7*, 982.
[94] G. E. Eperon, G. M. Paternò, R. J. Sutton, A. Zampetti, A. A. Haghighirad, F. Cacialli, H. Snaith, *J. Mater. Chem. A* **2015**, *3*, 19688.
[95] G. Mannino, I. Deretzis, E. Smecca, A. La Magna, A. Alberti, D. Ceratti, D. Cahen, *J. Phys. Chem. Lett.* **2020**, *11*, 2490.
[96] W. Shockley, H.-J. Queisser, *J. Appl. Phys.* **1961**, *32*, 510.